
Article:
Bean, Jonathan J. and McKenna, Keith P. orcid.org/0000-0003-0975-3626 (2016) Origin of differences in the excess volume of copper and nickel grain boundaries. Acta Materialia. pp. 246-257. ISSN 1359-6454

https://doi.org/10.1016/j.actamat.2016.02.040

Acta Materialia 110 (2016) 246–257

Contents lists available at ScienceDirect

Acta Materialia

journal homepage: www.elsevier.com/locate/actamat

Full length article

Origin of differences in the excess volume of copper and nickel grain boundaries

Jonathan J. Bean*, Keith P. McKenna

Department of Physics, Heslington, York, North Yorkshire, YO10 5DD, UK

ARTICLE INFO

Article history:
Received 12 January 2016
Received in revised form
18 February 2016
Accepted 18 February 2016
Available online 23 March 2016

Keywords:
Grain boundaries
Copper
Nickel
Excess volume
Atomistic modeling

ABSTRACT

The excess volume associated with grain boundaries is one of the primary factors driving defect segregation and diffusion which controls the electronic, mechanical and chemical properties of many polycrystalline materials. Experimental measurements of the grain boundary excess volume of fcc metals Cu and Ni have shown a difference of over 40%. The difference in lattice constant between Cu and Ni is only 3%, therefore this substantial difference is currently lacking explanation. In this article we employ a high throughput computational approach to determine the atomic structure, formation energy and excess volume of a large number of tilt grain boundaries in Cu and Ni. By considering 400 distinct grain boundary orientations we confirm that theoretically there is a systematic difference between the excess volumes in the two materials and we provide atomistic insight into the origin of the effect.

1. Introduction

Grain boundaries play a decisive role in determining the properties and functionality of polycrystalline materials relevant to wide ranging technological applications [1–5]. While grain boundary (GB) phenomena can be varied and complex there are some features that appear to be more universal with general implications for understanding the properties of polycrystalline materials. For example, GBs are almost always associated with an excess volume relative to the corresponding bulk crystal. This additional 'free space' is thought to be one of the main factors responsible for the preferential segregation of defects and impurities towards GBs, which affects key materials properties, such as mechanical strength and electrical resistivity [6–8]. It also helps explain the phenomena of enhanced impurity diffusion along GBs that has been observed in a diverse range of materials [9–11]. While excess volume is recognized as a key materials parameter probing it in real materials remains extremely challenging. A small number of studies have characterized excess volume for specific GBs using high-resolution electron microscopy [12,13]. More recently ensemble average excess volumes have been determined for bulk polycrystalline samples of copper and nickel using high-precision difference dilatometry [14,15]. These experimental studies found that the average excess volume associated with grain boundaries in Cu (0.46 Å) is significantly larger than that in Ni (0.32 Å) – a difference of over 40%. Given that Cu and Ni possess the same fcc crystal structure and fairly similar lattice constants (3.62 Å and 3.52 Å respectively – a difference of less than 3%) the origin of this distinct behavior is not well understood. An atomistic understanding of the nature and origin of GB excess volumes is lacking but could provide invaluable insights to guide the choice of materials for applications. Furthermore, identification of key properties that determine GB excess volumes would be very useful for materials design and optimization.

The structure and properties of GBs in metals have been the focus of many previous experimental and theoretical investigations [8,16–19]. Experimentally, high resolution transmission electron microscopy (TEM) has proven an invaluable probe of GB structure down to the atomic level. Detailed images of the structure of individual tilt GBs have also been acquired [20,21], confirming the existence of a relationship between the GB orientation and the structures of associated dislocation cores. Corresponding GB formation energies have also been estimated by analysis of triple junctions [22,23]. GB excess volumes are more challenging to probe directly but have been studied for both individual GBs and polycrystalline samples, in which case the excess volume corresponds to an average over many GB types [12–15]. Segregation of elements

* Corresponding author.
E-mail addresses: jonathan.bean@york.ac.uk (J.J. Bean), keith.mckenna@york.ac.uk (K.P. McKenna).

http://dx.doi.org/10.1016/j.actamat.2016.02.040

to GBs and their modified diffusion is also an issue that has received considerable attention [24–26]. For example, segregation of H and Bi to GBs in palladium and copper has been probed using techniques such as TEM and activity measurements [27,28]. The modified diffusion of impurities along GBs in metals have also been studied using the tracer diffusion method [10,29].

Theoretically, a range of modeling techniques based on both classical potentials and first principles calculations have been developed to predict the structure of GBs on the basis of their formation energy [30–37]. In many cases very good agreement with experiment is obtained for both structure and associated properties (e.g. mechanical, electronic or chemical) [30,33,35,38–40]. A rather general finding is that GBs are often favorable locations for the segregation of defects and impurities which in part has been associated with the additional 'free space' which can more easily accommodate lattice defects [39,41–43]. Often such calculations are performed at the classical potential level but in some cases first principles methods such as density functional theory are employed. For example, the segregation of He to GBs in metals and the resulting embrittlement has received significant attention owing to its relevance to the design of materials for fusion reactors [44–46]. While excess volume differences in otherwise similar metals (like Cu and Ni) have been observed experimentally, theoretical insight into this important issue is currently missing.

In this article we present a detailed theoretical investigation into GB excess volume in the polycrystalline metals Cu and Ni. These materials are chosen to allow comparison with extensive previous theoretical and experimental studies and due to their numerous applications in areas such as spintronics, fusion, fission, power generation and catalysis [47–50]. We focus our study on symmetric tilt GBs and cover a wide range GB orientations in order to draw out trends across both materials. By employing an automated computational approach based on an embedded atom model (EAM) description of interatomic interactions [33,51] we determine the stable structures of over 400 distinct symmetric tilt GBs for both Cu and Ni. We further demonstrate the validity of the approach by comparison to first principles calculations of GB properties using density functional theory. Our results recover a systematic difference in excess volume of between 0.1 and 0.2 Å in very good agreement with experimental data. By analyzing the strain at the atomic level we demonstrate that the excess volume difference is localized in a region of 5–10 Å around the GB plane. We provide a semi-quantitative explanation for the origin of the difference in terms of the differing bulk moduli of Cu and Ni (138 GPa and 186 GPa respectively). Altogether, these results provide much needed atomistic insight into the nature and origin of excess volume differences in Cu and Ni.

The rest of this paper is structured in the following way. In Sec. 2 we describe the computational methods employed to determine the structure, formation energy and excess volume of GBs both at the interatomic potential and first principles levels. In Sec. 3 we discuss results for the structure and excess volume of a wide range of GBs to illustrate the systematic trends and also provide detailed analysis of nature and origin of differences at the atomic level for a selection of GBs. Finally, in Sec. 4 and Sec. 5 the results are discussed and the main findings of the research summarized.

2. Methodology

2.1. General approach

Symmetric tilt GBs are two-dimensional extended defects that form at the interface between two grains symmetrically rotated about a common tilt axis. The crystallographic orientation of the GB can be fully defined by specifying the crystallographic plane parallel to the GB (*hkl*) and the tilt axis [*mno*] and is usually denoted in the form (*hkl*)[*mno*]. Here, we model the atomic structure of such GBs in three-dimensionally periodic supercells as shown in Fig. 1a. To make the supercell periodic in the direction perpendicular to the GB plane two identical GBs are introduced. We ensure that the separation between the GBs is sufficiently large that mutual elastic interactions are small and can be safely neglected in prediction of GB properties (we find GB separations of 30 Å are more than sufficient and this is the minimum separation employed throughout this study).

While the crystallographic orientation of the grains in the supercell are fully defined by the GB type – (*hkl*)[*mno*] – it is not known *a priori* how the grains should be positioned with respect to each other. In particular, it is known that GBs can exhibit rigid body translations where one grain is translated with respect to the other in the plane parallel to the GB (e.g. see Fig. 1b). To find the most stable GB structure we perform total energy calculations on supercells of the type shown in Fig. 1 and fully optimize the structures using the EAM to describe interatomic interactions. First principles calculations within the framework of density functional theory are also performed on a smaller subset of structures identified by the initial EAM screening. Details of both of these approaches are given in the following sections.

To identify the most stable GB structure for a given orientation we systematically generate a large number of initial structures corresponding to different relative translations of one grain with respect to the other. Translations are performed in steps of 1 Å over a range of half of the supercell length in the periodic directions [*mno*] and [*hkl*]×[*mno*] (the vector orthogonal to (*hkl*) and [*mno*]) and between −0.5 and +0.5 Å in the GB normal direction (*hkl*). It has been found that the lowest energy structures can be found using only three translation states in (*hkl*) as all inequivalent interface configurations can be explored via translations in (*hkl*) × [*mno*] and [*mno*]. Following crystal translation, if any two atoms are closer than 0.1*a* (where *a* is the lattice constant) one is deleted to obtain a more realistic starting configuration for geometry optimization. This algorithm generates a large number of initial structures corresponding to different grain terminations, relative grain translations and atom configurations near the

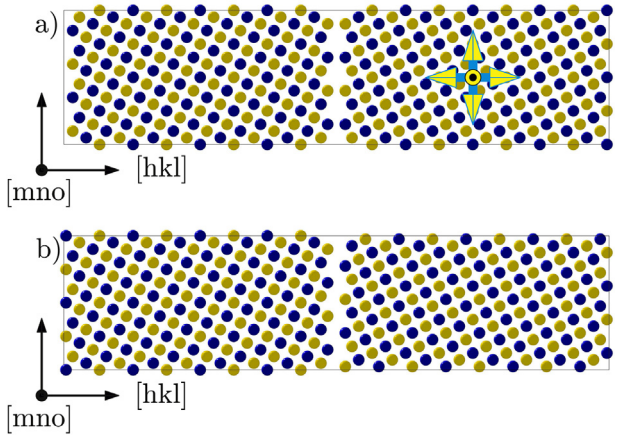

Fig. 1. A typical bicrystal supercell in an fcc material. The yellow and blue atoms indicate atoms in different planes perpendicular to the tilt direction [*mno*]. a) Initially two mirror symmetric grains are placed in the simulation cell. The arrows indicate the directions in which the right grain is to be translated. b) An example of a configuration obtained after one crystal is translated with respect to the other. (For interpretation of the references to colour in this figure legend, the reader is referred to the web version of this article.)

interface. The initial structures generated using the procedure outlined above are fully optimized with respect to relaxation of all ions and the length of the supercell perpendicular to the grain boundary using the conjugate gradients method [52–54]. This procedure is very similar to that we and others have applied in previous work on a range of materials including TiO_2, MgO and HfO_2 [55–57]. Following relaxation the forces on all atoms in the supercell are less than 1×10^{-8} eV/Å and each optimized structure corresponds to a well defined potential energy minimum. The stability of each GB structure is then quantified by its formation energy,

$$\gamma = (E_{tot} - NE_{coh})/2A, \quad (1)$$

where E_{tot} is the optimized total energy of the supercell, N is the number of atoms in the supercell, E_{coh} is the bulk cohesive energy and A is the cross-sectional area of the supercell. The most stable GB is then identified as the structure with the lowest formation energy for which we compute the associated excess volume defined as,

$$\delta V = (V_{tot} - N\Omega_{bulk})/2A, \quad (2)$$

where V_{tot} is the volume of the supercell and Ω_{bulk} is the volume per atom in the bulk crystal. One advantage of this approach is that it is suited to high-throughput calculations which can be efficiently implemented for high performance multi-processor supercomputers. For this work we have implemented the algorithm within the Large-scale Atomic/Molecular Massively Parallel Simulator (LAMMPS) code [58].

2.2. Embedded atom method

As described above stable GB structures are initially identified by describing interatomic interactions using the EAM. This approach offers a balance between physical accuracy and computational feasibility, allowing for high-throughput calculations on many millions of supercells to be performed. Extensive research undertaken on transition metals has demonstrated that EAM potentials give an accurate description of many bulk, surface, GB and defect properties [59–62]. In general the total energy of a system of metal atoms is described within the EAM method in the following way,

$$E_{\mathrm{tot}} = \frac{1}{2}\sum_{i,j} V(r_{ij}) + \sum_i F_i(\rho_i), \quad (3)$$

$$\rho_i = \sum_j \Phi(r_{ij}), \quad (4)$$

where $V(r_{ij})$ is a pair potential term which depends on the separation between atoms i and j and F_i is the embedding energy function for atom i. The latter term accounts for the many-body aspects of the atomic binding and is expressed in terms of a sum over atom centered functions $\Phi(r_{ij})$ which phenomenologically represent the shape of the electron density around a particular atom. Different EAM implementations differ in the choices made for each of these functions which may be either expressed in an analytic functional form (together with a set of parameters) or they can be tabulated numerically. These parametrizations are usually determined by fitting either to experimental data and/or first principles calculations.

Numerous EAM potentials have been developed for Cu and Ni and so we have performed a systematic investigation of properties predicted by the methods to determine the most appropriate to employ in this study. We have assessed the ability of different potentials to describe bulk properties such as the lattice constant, the cohesive energy, the bulk moduli as well formation energies of low-index surfaces. All calculations have a precision of 1×10^{-6} eV for total energies and <0.001 Å for excess volumes. The bulk moduli and lattice constants are calculated by fitting the volume dependence of total energy to the Birch–Murnaghan equation of state [63]. Surfaces are modeled using a similar approach to the one described for GBs in Sec. 2.1 however only one grain (more commonly referred to as a slab in surface calculations) is included and periodic boundary conditions are employed only in the directions parallel to the surface. The surface energy is defined in the same way as the GB formation energy using Eq. (1) and surface energies have been fully converged with respect to slab thickness.

Table 1 summarizes properties calculated using a range of potentials for Cu and Ni. These include the Sutton and Chen (SC) [61], Cleri and Rosato (CR) [60], Ackland [59] and Mendelev [64]. We find the Ackland potential describes the properties of copper more accurately than the others. This potential is fitted to the lattice parameter a_0, three important elastic constants C_{11}, C_{12}, C_{44}, the cohesive energy E_{coh} and the unrelaxed vacancy formation energy. The Ackland potential has a cut-off value $r_c = 4.43$ Å for copper. Results for this potential can be found in Table 1. For nickel we have found the Mendelev potential describes the properties more accurately. This is initially parameterized in the same way as the Ackland potential, however the weighting of the solid properties is reduced in order to allow the system to describe the liquid phase. The Mendelev potential has a cut-off value $r_c = 6.0$ Å for nickel.

2.3. Density functional theory

We perform first principles calculations on GB supercells obtained from our EAM screening within the formalism of density functional theory (DFT) [69,70]. Calculations have been performed using the Cambridge serial total energy package (CASTEP) [71]. Ultrasoft pseudopotentials model the inner electrons and 3*d* and 4*s* valence electrons are treated explicitly. The generalized gradient approximation (GGA) with the parameterization of Perdew, Burke and Ernzerhof (PBE) has been used to describe the exchange correlation energy [72]. To determine the bulk properties of the metals the wavefunctions are expanded in a plane-wave basis with energies up to 500 eV and a Monkhorst-Pack k-point grid of $12 \times 12 \times 12$ for primitive cells and structures are optimized using the limited-memory Broyden Fletcher Goldfarb Shanno (LBFGS) algorithm [73]. For GB structures we reduce the plane-wave basis cut-off to 350 eV and employ Monkhorst-Pack k-point grids of $1 \times 3 \times 3$ (with only one k-point along the non-periodic GB normal

Table 1
Summary of properties calculated using various embedded atom method potentials for Cu and Ni. E_{coh} (eV) is the cohesive energy, a_0 (Å) is the lattice constant, B_0 (GPa) is the bulk modulus and γ_{hkl} (Jm^{-2}) is the surface energy relating to surface (hkl).

Cu	Expt.	DFT	SC	Ack.	CR
E_{coh}	−3.54 [65]	−3.70	−3.49	−3.52	−3.54
a_0	3.62 [66]	3.63	3.62	3.62	3.61
B_0	138 [67]	139	135	144	142
γ_{001}		1.33	1.22	1.14	1.36
γ_{011}		1.48	1.29	1.23	1.47
γ_{111}		1.25	1.14	0.95	1.27
Ni	**Expt.**	**DFT**	**SC**	**Mend.**	**CR**
E_{coh}	−4.44 [65]	−4.92	−4.43	−4.39	−4.43
a_0	3.52 [66]	3.52	3.52	3.52	3.52
B_0	186 [68]	200	192	174	186
γ_{001}		2.30	1.64	1.41	2.62
γ_{011}		2.35	1.73	1.59	2.78
γ_{111}		1.97	1.53	1.28	2.60

direction). The EAM optimized supercells have in-plane dimensions corresponding to the EAM optimized bulk lattice constants. These supercells must be scaled to reflect the optimized DFT lattice constant which in general may differ slightly. GB formation energies have been calculated by comparing the total energy difference between a supercell containing a GB and a bulk supercell of the same size. This minimizes the error associated with differing *k*-point sampling and basis sets. Surface energies are calculated with a *k*-point grid of $1 \times 9 \times 9$, $1 \times 8 \times 8$ and $1 \times 6 \times 4$ for (100), (110) and (111) surfaces respectively with a cut-off energy of 500 eV. The DFT predicted bulk and surface properties are included in Table 1 and comparison with the EAM potential and experimental values demonstrates good agreement across the board.

3. Results

3.1. Determination of grain boundary structure and properties

In this section we illustrate our approach for determining the stable structures of arbitrary symmetric tilt GBs by describing a number of examples in detail. First we consider the Σ5 Ni(210)[001] GB for which our systematic screening approach identifies three inequivalent low formation energy structures as shown in Fig. 2. We label these structures a–c ordered according to their formation energy. The most stable GB structure Ni(210)[001]-a ($\gamma = 1.38$ Jm^{-2}) has no rigid body translation between the two crystals and is fully symmetric about the interfacial plane. The GB can be viewed as a periodic arrangement of triangular structural units as indicated in the figure. The next most stable structure Ni(210)[001]-b ($\gamma = 1.43$ Jm^{-2}) is formed from diamond shaped structural units. Finally GB structure Ni(210)[001]-c ($\gamma = 1.70$ Jm^{-2}) has one grain which has a rigid body translation of $a/2[\bar{1}20]$ with respect to the other and is not mirror symmetric. The GB can be viewed as a periodic arrangement of two irregular quadrilaterals.

To further verify our approach we have determined stable structures for the Σ3 (111)[101], Σ3 (121)[101] and Σ5 (210)[001] symmetric tilt GBs in Cu and Ni in a similar way. We note that the (111)[101] GBs in the fcc materials copper and nickel corresponds to a twin boundary with a very low formation energy, and this is confirmed by the systematic screening approach. Table 2 summarizes the calculated formation energies and excess volumes for 3 GB at both the EAM and DFT levels of theory. The DFT and EAM determined GB formation energies are in general very similar and predict the same relative stability of the three GB types for each material. The calculated excess volumes again differ more significantly (with the DFT values being in general lower) however again the relative ordering is consistent. The only exception is the

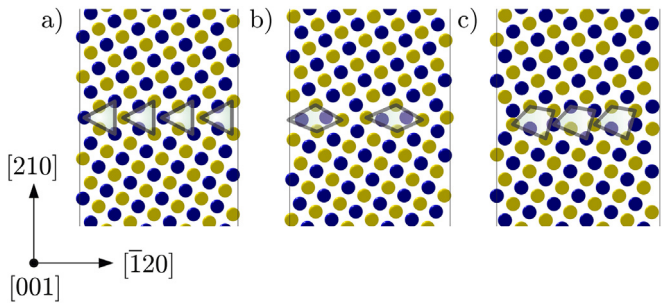

Fig. 2. Optimized structures of the nickel (210)[001] grain boundary. The yellow and blue atoms indicate atoms in different planes perpendicular to the tilt direction [001], with the structural units highlighted. The three most stable GB structures are shown (a–c). (For interpretation of the references to colour in this figure legend, the reader is referred to the web version of this article.)

Table 2
Comparison of EAM and DFT predictions of excess volume δV (Å) and grain boundary formation energy γ (Jm^{-2}) for a number of tilt GBs in Cu and Ni.

Cu	γ_{DFT}	γ_{EAM}	δV_{DFT}	δV_{EAM}
(111)[101]	0.02	0.02	0.01	0.04
(121)[101]	0.57	0.77	0.17	0.29
(210)[001]-a	0.92	0.96	0.24	0.36
(210)[001]-b	0.86	1.07	0.34	0.36
Ni	γ_{DFT}	γ_{EAM}	δV_{DFT}	δV_{EAM}
(111)[101]	0.04	0.10	0.01	0.02
(121)[101]	0.84	1.02	0.10	0.07
(210)[001]	1.23	1.38	0.35	0.36

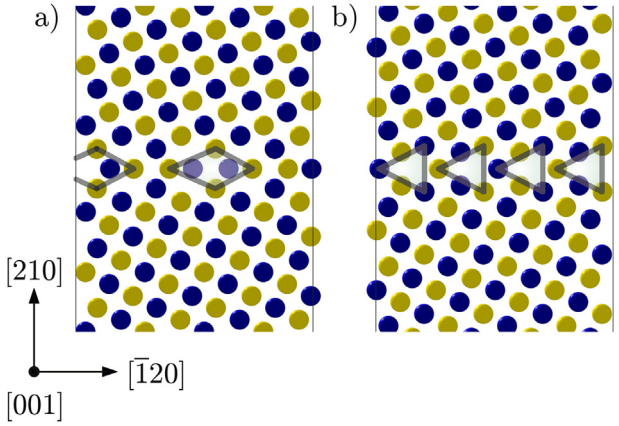

Fig. 3. Optimized structures of the copper (210)[001] grain boundary. The yellow and blue atoms indicate atoms in different planes perpendicular to the tilt direction [001], with the structural units highlighted. The two most stable GB structures are shown (a–b). (For interpretation of the references to colour in this figure legend, the reader is referred to the web version of this article.)

Σ5 Cu(210)[001] GB for which the DFT and EAM approaches predict different structures as the most stable. Fig. 3 shows the two alternative structures of the Cu(210)[001] GB. Structure Cu(210)[001]-a ($\gamma = 0.96$ Jm^{-2}) is mirror symmetric and consists of a periodic arrangement of diamond structural units. Structure Cu(210)[001]-b ($\gamma = 1.07$ Jm^{-2}) is also mirror symmetric and consists of a periodic arrangement of triangular structural units. The energetic ordering of these two possible interfaces is swapped at the DFT level (Table 2) however the difference in energy remains very small 0.06 Jm^{-2} at the DFT level and 0.11 Jm^{-2} at the EAM level. This suggests that thermodynamically both structures may coexist, also observed by Vitek and Wang [74–78].

GB formation energies calculated using the EAM approach are in general higher than those calculated using DFT (by up to 0.2 Jm^{-2}). However, the relative ordering of formation energies is broadly consistent at both levels of theory. For example, the formation energy of Ni GBs is systematically higher than that of equivalent Cu GBs calculated using both EAM and DFT (Table 2). Likewise, while the absolute GB excess volume differs at the DFT and EAM levels of theory (by up to 0.12 Å) the relative ordering is again consistent. This suggests both EAM and DFT can predict relative differences in formation energy and excess volume between Cu and Ni reliably but not quantitatively. In the following we use the EAM since its lower computational expense allows us to consider a far greater number of GB structures and elucidate systematic trends. We note that achieving quantitative agreement with experiment on the average GB excess volume would be much more challenging and would require knowledge of the precise distribution of GBs in materials. The results in Table 2 are also consistent with previous

studies demonstrating the reliability of the approach [30,33,35,78–83].

3.2. Excess volume in Cu and Ni

The methodology described in the previous sections is applied to consider a series of GBs of the general type (*hkl*)[*mno*] in Cu and Ni. GB planes which are perpendicular to the tilt axis define tilt GB supercells for which the most stable structure is determined. We consider supercells defined by the integers *h*,*k*,*l*,*m*,*n* and *o* ranging from 1 to 20 and all those with less than 15,000 atoms are considered for structural optimization (400 distinct orientations for each material). In Fig. 4 we show the correlation between the GB formation energy and the excess volume across all of these orientations for both Cu and Ni. Broadly speaking there is a linear correlation between GB formation energy and excess volume which becomes pronounced in the low formation energy limit, in agreement with previous theoretical calculations [84]. However we observe that there is a stark difference between the range of excess volumes in Cu and Ni, with Cu being on average 40% larger.

The variation of excess volume with respect to GB orientation can be illustrated by mapping each GB orientation onto a unit sphere [30,85]. Once in spherical coordinates a projection on to a circle using a Lambert azimuthal equal area projection can be performed [86]. The methodology for the construction of this projection is given in the supplemental material. Fig. 5 shows the result for Cu and Ni, recognizing that due to symmetry it is only necessary to show an irreducible sector of the circle. We note that the set of 400 GB orientations considered span the perimeter and most of the area inside this irreducible sector. Fig. 5 also helps further highlight that the excess volume is systematically larger in Cu than Ni.

Paths between particular high symmetry orientations (labeled A to F in Fig. 5) define a series of GBs with fixed tilt axis [*mno*] (known as a tilt series). For example, the [100] tilt series is defined by the path AC. The degree of rotation of the two grains can be expressed by the tilt angle,

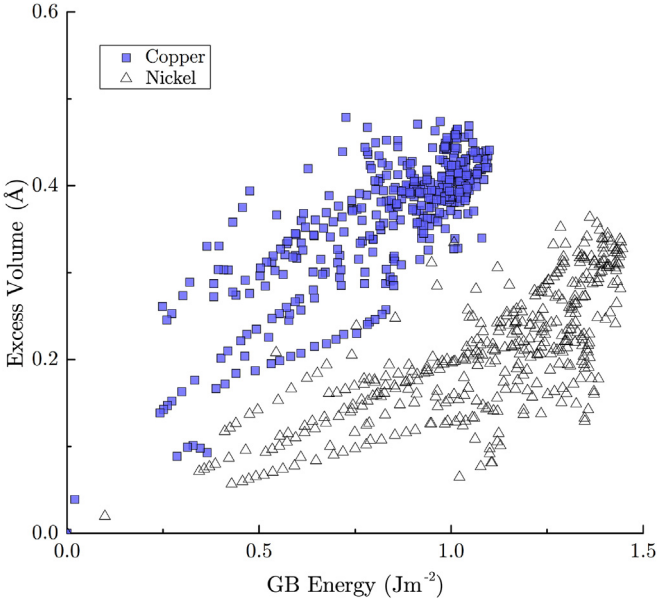

Fig. 4. Correlation between grain boundary formation energy (Jm^{-2}) and excess volume (Å) for 400 unique stable GBs in Cu and Ni. Cu is systematically higher in excess volume than Ni.

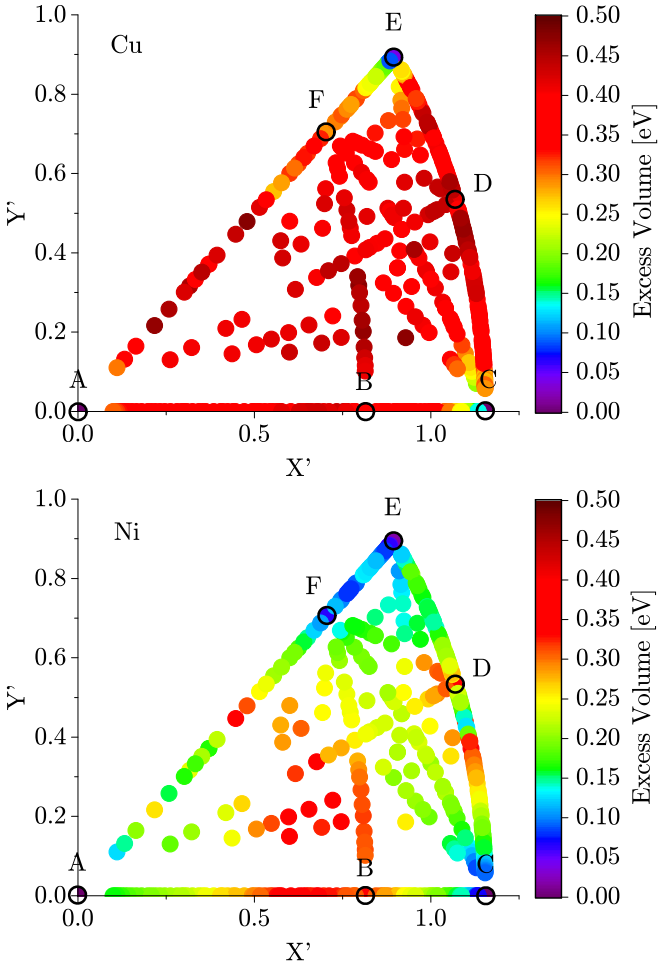

Fig. 5. Lambert azimuthal projection showing the variation of excess volume with GB orientation for Cu and Ni. X′ and Y′ are coordinates in this projection which represent a mapping from the Miller index definition (*hkl*)[*mno*] (see supplemental material for definition). High symmetry orientations are labeled on the figure as follows: A ((100)[001]), B ((210)[001]), C ((101)[010]), D ((212)[101]), E ((111)[101]) and F ((131)[101]).

$$\alpha = \cos^{-1}\left(\frac{|oh - mk|}{\sqrt{(m^2 + o^2)(h^2 + k^2 + l^2)}}\right), \tag{5}$$

where *h*, *k*, *l*, *m* and *n* are the indices characterizing the GB orientation (*hkl*)[*mno*]. The variation of excess volume with tilt angle for four high-symmetry tilt series: [100] (path AC), [101] (path CEA), [111] (path CF) and [201] (path ADFB) is shown in Fig. 6. Each tilt series exhibits a characteristic dependence on tilt angle with local minima appearing at particular GB orientations of high symmetry. For example, near 36° in the [001] tilt series (Σ 5 (310)[001]) or near 70° in the [101] tilt series (Σ 3 (111)[101]). This mirrors the cusp behavior that is well known in the variation of GB formation energy with tilt angle [30,33]. Importantly, while the trend in each series is similar for both Cu and Ni there is a systematic difference of up to 0.2 Å, consistent with experimental results for polycrystalline materials containing more general GBs [14,15]. Only for a small number of low index GB orientations is the difference absent – for example Σ 5 (210)[001] in the [001] tilt series – which we attribute to its much higher symmetry which constrains atomic relaxation near the interface.

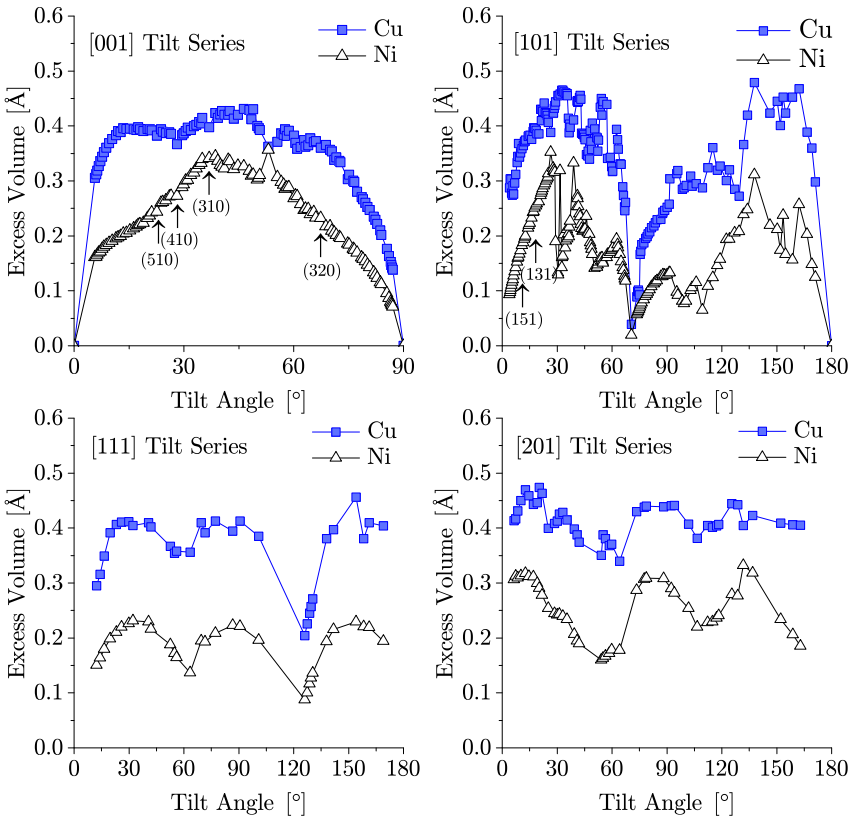

Fig. 6. Variation of excess volume with tilt angle for the four high-symmetry tilt series: [100, 101, 111] and [201]. While the trend in each series is similar for both Cu and Ni there is a systematic difference of up to 0.2 Å.

3.3. Origin of excess volume differences in Cu and Ni

The results presented in Sec. 3.2 clearly demonstrate that there is a systematic difference between the excess volumes of Cu and Ni tilt GBs, larger than would be expected based on their rather similar lattice constants (differing by less than 3%). However, the above analysis above does not allow us to assess whether this difference is associated with the local atomic structure at the interface or with the longer range strain field associated with GBs. To provide insight into this question requires a detailed analysis of the atomic structure of GBs in both materials. For this purpose we select a number of GBs from the [001] and [101] tilt series for more detailed analysis. In particular, the Σ 5 (310)[001], Σ 17 (410)[001], Σ 13 (510)[001], Σ 13 (320)[001], Σ 11 (131)[101] and Σ 27 (151)[101] GBs as indicated by the arrows in Fig. 6. Fig. 7 shows the local atomic structures of each of these GBs for both Cu and Ni. In each case the structural units which define the interface structure extend to the second atomic layer from the plane of mirror symmetry. We calculate the perpendicular distance from the mirror plane to the second atomic layer, $d_{Cu/Ni}$, to quantify the half-width of the structural unit (shown for each GB in Fig. 7).

The half-widths of the structural units in (310)[001], (410)[001], (510)[001], (131)[101] and (151)[101] GBs are all larger in Cu than Ni (0.020 Å, 0.070 Å, 0.072 Å, 0.095 Å and 0.12 Å respectively) which is consistent with the observed excess volume differences. These differences are sufficient to account for a significant proportion of the total difference in excess volume observed. However, we find that in (320)[001] the difference is −0.065 Å, meaning that the long range strain field plays a larger role in the determination of the total excess volume. We have also analyzed differences in structural units for an additional six GBs (see Supplemental Material) finding very similar results. We note a direct comparison of the widths of structural units in Cu and Ni GBs is only possible in cases where the most stable GB structure in each material is equivalent. Of the twelve GBs analyzed the half-width of the structural unit is larger in Cu than Ni for ten GBs. However, in all cases longer range strain (i.e. beyond the second atomic layer away from the GB plane) is needed to explain differences in excess volume between Cu and Ni.

To analyze the longer range differences in atomic structure between Cu and Ni GBs of the same orientation we define the following dimensionless quantity,

$$\Delta = \left(\frac{d_{Cu}}{a_{Cu}} - \frac{d_{Ni}}{a_{Ni}}\right), \tag{6}$$

where $d_{Cu/Ni}$ is the perpendicular distance from the mirror plane to a particular atomic layer in the supercell (similar to the definition above but for a general atomic layer), and a_{Cu} and a_{Ni} are the lattice constants of Cu and Ni. Far from the GB atomic planes are equally spaced and do not contribute to the excess volume, i.e. $d_{Cu} \rightarrow \delta V_{Cu} + k a_{Cu}$ and $d_{Ni} \rightarrow \delta V_{Ni} + k a_{Ni}$, where $\delta V_{Cu/Ni}$ is the excess volume and k is a constant. Far from the GB Δ converges to a constant ($\Delta = \delta V_{Cu}/a_{Cu} - \delta V_{Ni}/a_{Ni}$). Therefore the variation of Δ provides a convenient way to quantify the spatial extent of the region around the GB that contributes to the excess volume difference.

In Fig. 8 we show how Δ varies for each of the GB identified above. We note that in each case the second point corresponds to the distance to the second plane shown in Fig. 7. Considering the (310)[001] GB one finds that for the second layer Δ is negative, consistent with the small difference in the structural unit half-width noted above. However, Δ exhibits oscillations from layer to layer converging to a positive value by the eleventh atomic plane

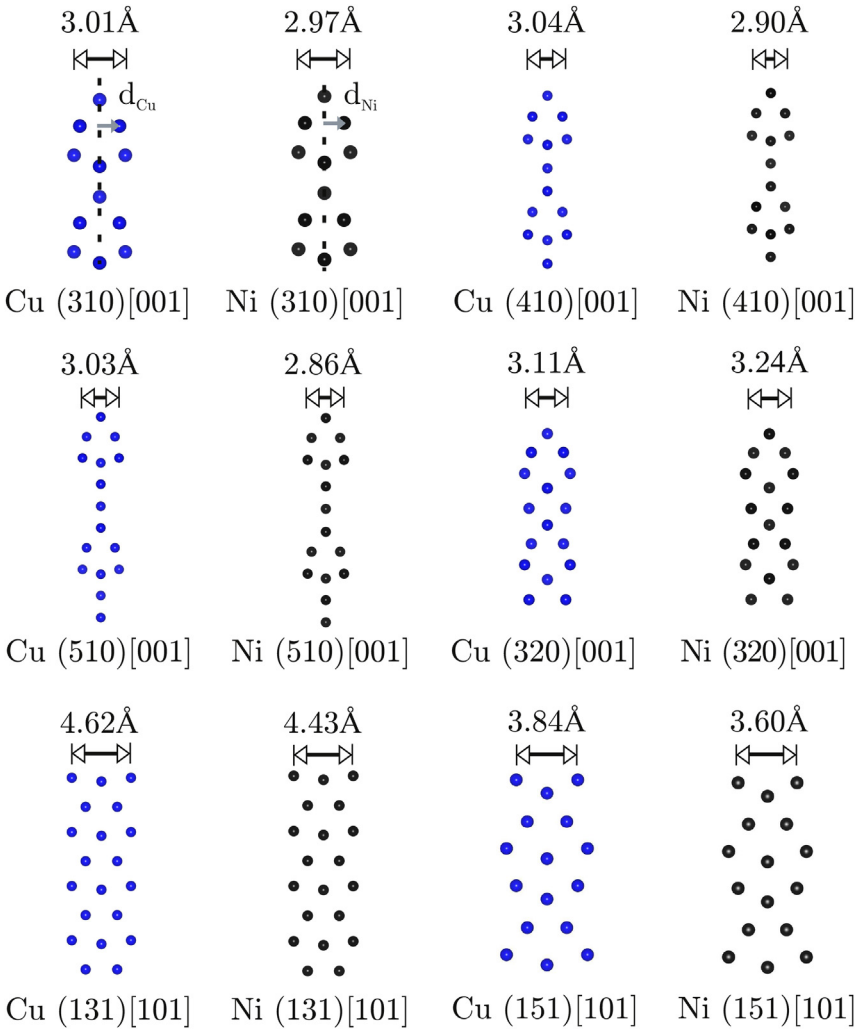

Fig. 7. Atomic structure of selected grain boundaries in the [100] and [101] tilt series. The half-width of each structural unit (defined as the perpendicular distance from the mirror plane to the second atomic layer) is shown for each GB in Cu and Ni.

(corresponding to a distance of about 6 Å). Similar oscillations are seen in the other GBs considered with convergence to a positive Δ typically being achieved within around 5 to 15 Å of the GB plane. However, in cases with a longer range of convergence the variation of Δ exhibits small amplitude oscillations characteristic of a strain field and the majority of the excess volume is already established within a smaller range of about 5 Å.

The above analysis indicates that the differences in GB excess volume between Cu and Ni are associated with differences in the local atomic structure near the GB, mainly within a range of ±5 Å of the GB plane but with smaller strain contributions extending up to 15 Å in some cases. This difference cannot be explained by the difference in the lattice constants of Cu and Ni and ultimately must be due to differences in the interatomic interactions.

3.4. Analysis of bond strain

Further analysis of the atomic structures obtained in this study indicates that in the regions near GBs bonds can be strained significantly compared to the bulk. In extreme cases bonds can be compressed by up to 10% and extended by up to 15%. However, the majority of bonds lie in a range of ±2% strain. To understand how bond strains differ in Cu and Ni GBs all of the first nearest neighbor distances within 10 Å of the interface have been calculated for the (310)[001], (410)[001], (510)[001], (320)[001], (131)[101] and (151)[101] GBs. Due to symmetry only one side of the grain is considered. The strain σ for each bond is calculated using the following formulas,

$$\sigma_{Cu} = \frac{l_{Cu} - \frac{\sqrt{2}}{2}a_{Cu}}{\frac{\sqrt{2}}{2}a_{Cu}}, \tag{7}$$

$$\sigma_{Ni} = \frac{l_{Ni} - \frac{\sqrt{2}}{2}a_{Ni}}{\frac{\sqrt{2}}{2}a_{Ni}}, \tag{8}$$

where l_{Cu} and l_{Ni} are the lengths of each bond in Cu and Ni respectively, σ_{Cu} and σ_{Ni} are the strains in Cu and Ni respectively and the factor of $2/2a$ arises from calculating the nearest neighbor distance in an fcc metal from the lattice constant. The difference of the strains η is defined below,

$$\eta = \sigma_{Cu} - \sigma_{Ni}. \tag{9}$$

This difference is calculated for each bond and plotted in a histogram with a bin width of 0.25% for the whole population of bonds within 10 Å of the interface and a reduced sample in which

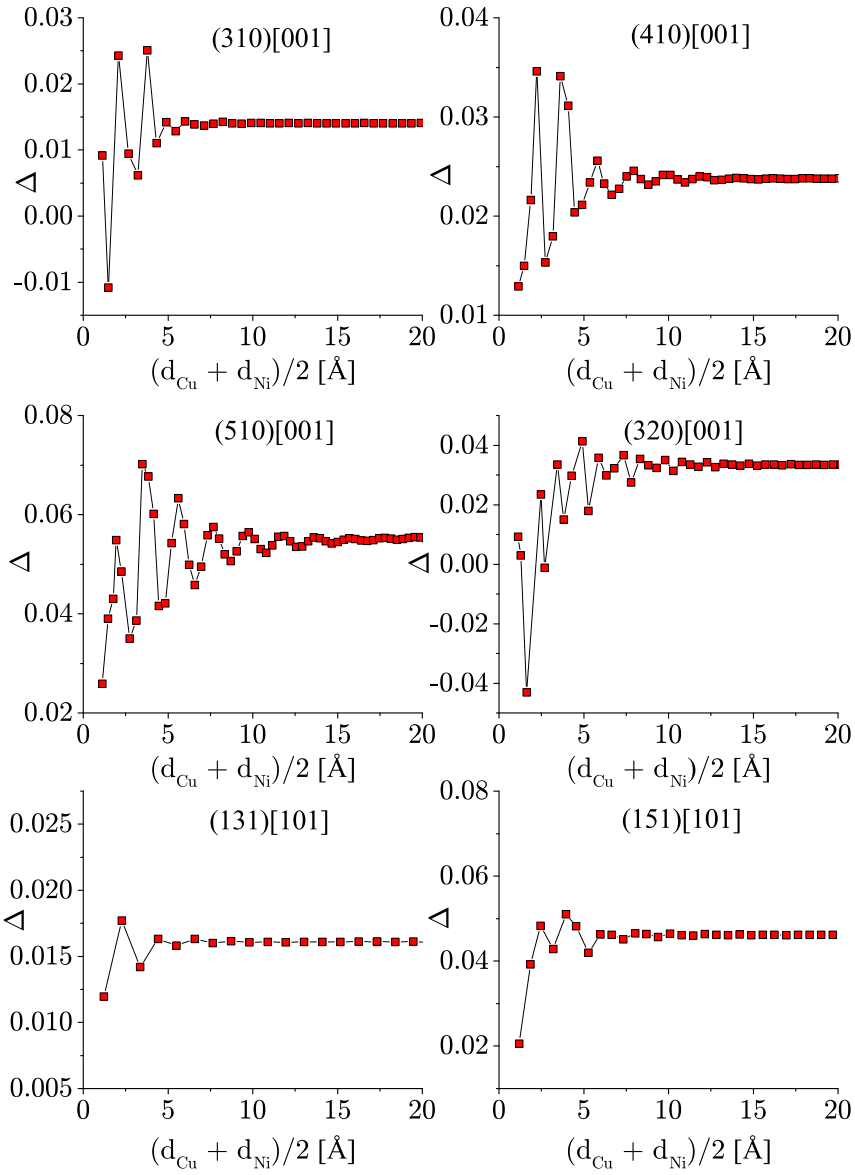

Fig. 8. Variation of the dimensionless parameter Δ (Eq. (6)) with distance from the GB mirror plane for GBs from the [100] and [101] tilt series. The convergence of Δ to a positive value within 5–15 Å of the mirror plane defines the region associated with the excess volume.

only strains greater than 1% are allowed $|\sigma| > 1\%$. For values greater than zero η characterizes a bond which is strained more in Cu than in Ni, for values less than zero η describes a bond which is strained more in Ni than Cu. The reduced range is taken to reduce the skew of the distribution towards zero since for bulk like bonds there is no preferential straining. The histograms show that there are far more bonds with $\eta > 0$, which suggests that on average Cu is strained more than Ni, this is further emphasized in (Fig. 9 & Fig. 10). This is consistent with the fact that the bulk modulus of Cu is considerably smaller than that of Ni (138 GPa compared to 186 GPa) a property well represented by the EAM potentials used. Therefore the difference in bulk moduli provides a semi-quantitative interpretation for the observed difference in excess volume between Cu and Ni.

4. Discussion

The primary factors which may affect the validity of our predictions are the accuracy and transferability of the EAM potentials and the suitability of the approach employed to determine the most stable structure for a given GB orientation. Comparisons between DFT and EAM predicted bulk and GB properties suggest EAM potentials provide a reasonable description although improvements could be made to the potentials to more accurately model highly strained bonds (−15% / + 10%) in GBs which may not be as well described.

Furthermore to accurately predict stable structures GB supercells must also be large enough such that the two GBs in the supercell do not interact with each other. Here we employ crystals of thickness 30 Å which we have found are sufficient to minimize such effects. We also ensured the number of points considered in the rigid body translations is sufficiently large that the most stable GB structures were found. The optimum grid size was found to be 1.0 Å parallel to the GB plane and 0.5 Å in the GB normal direction. However, it should be noted that while we have demonstrated through a number of examples that our approach can identify stable GB structures we cannot exclude the possibility that more

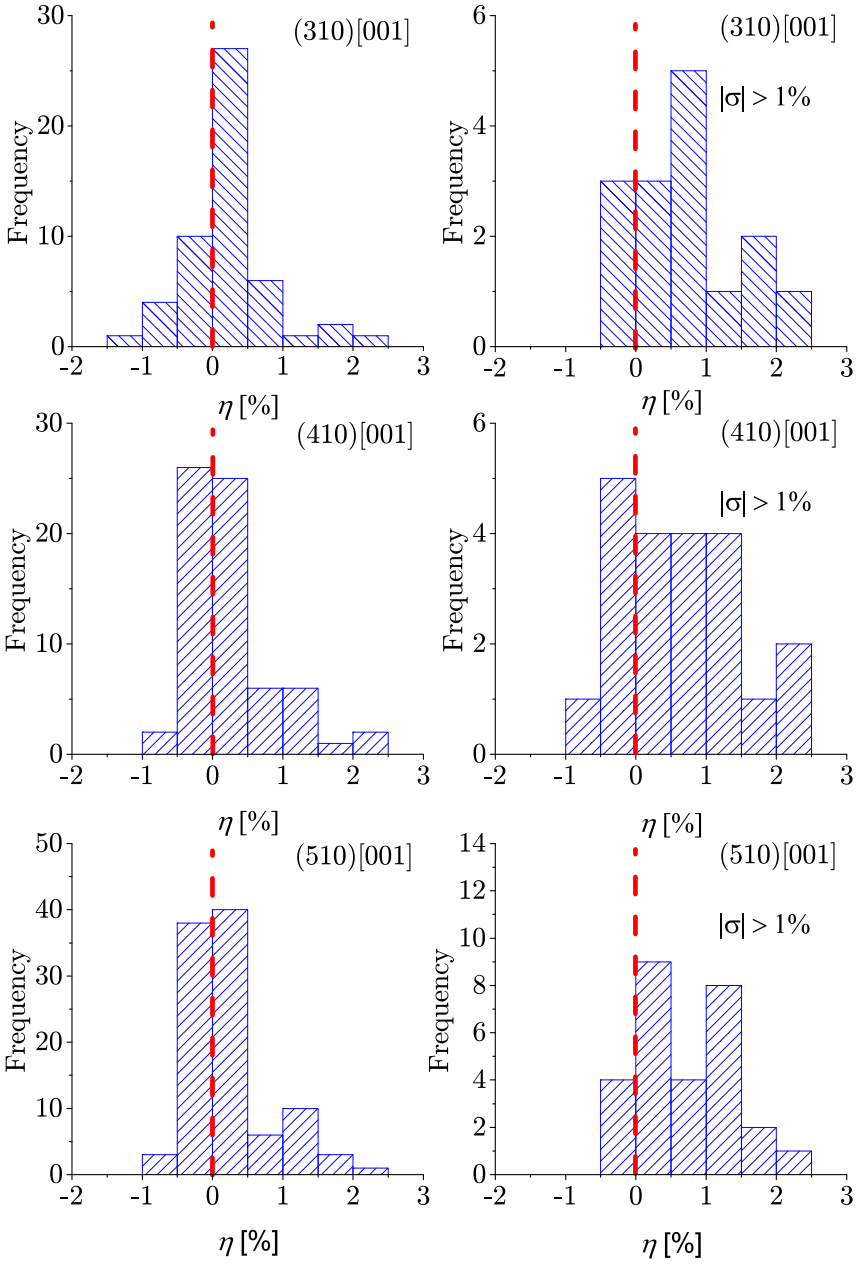

Fig. 9. Histograms of the strain difference η (Eqn. (9)) plotted with a bin width of 0.25%. The red dashed line indicates the parity value of the two strains ($\eta = 0$). There is a preference towards additional strain in Cu over Ni in all GBs. (For interpretation of the references to colour in this figure legend, the reader is referred to the web version of this article.)

stable structures may exist. Here, we have used a grid method to find stable structures but other approaches, such as displacement shift complete method (DSC) as described by Sutton and Ballufi [87], are also possible.

While this study is focused on symmetric tilt grain boundaries in principle the approach could be extended to more general types including asymmetric and mixed tilt/twist GBs. However, since the nature and origin of the effect (i.e. the presence of structural units at GBs and associated atomic relaxation and strain) is rather generic we do not expect the qualitative conclusions to differ significantly. We also note that even though the polycrystalline materials studied experimentally are likely to include a wide range of GB types, the tilt GBs we have studied provide very similar excess volumes for Cu and Ni.

5. Summary and conclusion

In this paper a high throughput method for predicting stable GB structures from a large number of initial configurations containing many thousands of atoms has been employed. The increased computational power now available has allowed simulation of over 400 unique tilt GB structures for Cu and Ni which span a wide range of orientations. Through analysis of these structures we have shown that there is a systematic difference between the excess volumes of Cu and Ni GBs of up to 0.2 Å which is consistent with experiment but not fully explained by the relatively small lattice constant difference of 3%. We find that the majority of the difference in excess volume occurs in the first 5 Å of the interface, with longer range strain effects contributing over a larger region. These

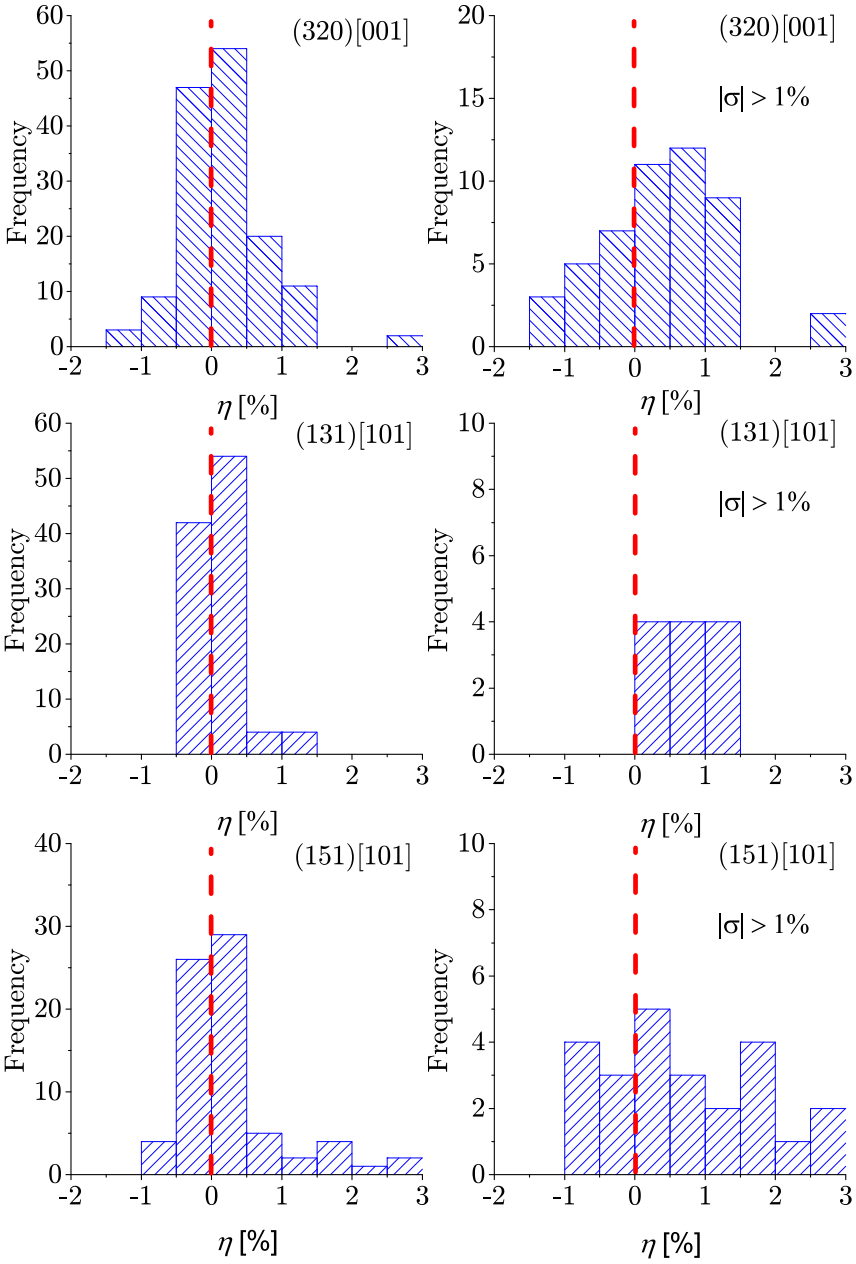

Fig. 10. Histograms of the strain difference η (Eqn. (9)) plotted with a bin width of 0.25%. The red dashed line indicates the parity value of the two strains ($\eta = 0$). There is a preference towards additional strain in Cu over Ni in all GBs. (For interpretation of the references to colour in this figure legend, the reader is referred to the web version of this article.)

differences can be understood as a result of the much smaller bulk modulus of Cu compared to Ni which means that bonds are easier to strain.

These results bring much needed insight into the nature of excess volume in metals and the reasons for the different behavior in the otherwise similar materials Cu and Ni. These ideas may find important application in the computational design of materials, for example by identifying materials properties which may influence excess volume. In particular, it is thought that GBs with higher excess volumes are significantly more prone to defect segregation, diffusion and embrittlement which may prove catastrophic when used in extreme environments such as fusion reactors [27,47]. If one wishes to minimize excess volume in metals in order to limit impurity segregation the results presented in this paper suggest that one should seek a material with a relatively small lattice constant and a large bulk modulus in addition to satisfying any other design criteria.

Polycrystalline materials are ubiquitous both in nature and manmade devices and the presence of GBs is known to affect many material properties [6–8]. Although experimentally the average excess volume of polycrystals have been measured by difference dilatometry, probing the excess volumes associated with individual GBs is more difficult [14,15]. The results presented in this paper provide atomic insight into the nature and origin of excess volume difference and provide an explanation for the different behavior of Cu and Ni observed experimentally.

Acknowledgments

We would like to thank Dr. Phil Hasnip for useful discussions involving CASTEP. We would also like to acknowledge financial support from the EPSRC (EP/K003151) and facilities support from the N8 Consortium (Polaris supercomputer), Materials Chemistry Consortium (Archer supercomputer, EPSRC grant EP/L000202). All data created during this research are available by request from the University of York Research database http://dx.doi.org/10.15124/ae1c1f4c-b6a7-4309-b904-a2525d3f02c3.

Appendix A. Supplementary data

Supplementary data related to this article can be found at http://dx.doi.org/10.1016/j.actamat.2016.02.040.

References

[1] L. Kazmerski, Polycrystalline and Amorphous Thin Films and Devices, Elsevier, 2012.
[2] T. Kamins, Polycrystalline Silicon for Integrated Circuit Applications, vol. 45, Springer Science & Business Media, 2012.
[3] R.S. Balmer, J.R. Brandon, S.L. Clewes, H.K. Dhillon, J.M. Dodson, I. Friel, P.N. Inglis, T.D. Madgwick, M.L. Markham, T.P. Mollart, N. Perkins, G.A. Scarsbrook, D.J. Twitchen, A.J. Whitehead, J.J. Wilman, S.M. Woollard, Chemical vapour deposition synthetic diamond: materials, technology and applications, J. Phys. Condens. Matter 21 (36) (2009) 364221.
[4] G. Palumbo, E.M. Lehockey, P. Lin, Applications for grain boundary engineered materials, JOM 50 (2) (1998) 40–43.
[5] E.M.C. Fortunato, P.M.C. Barquinha, A.C.M.B.G. Pimentel, A.M.F. Gonçalves, A.J.S. Marques, L.M.N. Pereira, R.F.P. Martins, Fully transparent ZnO thin-film transistor produced at room temperature, Adv. Mater. 17 (5) (2005) 590–594.
[6] A. Mayadas, M. Shatzkes, Electrical-resistivity model for polycrystalline films: the case of arbitrary reflection at external surfaces, Phy. Rev. B 1 (4) (1970) 1382.
[7] J.P. Hirth, The influence of grain boundaries, Metall. Trans. 3 (12) (1972) 3047–3067.
[8] C.T. Liu, C.L. White, J.A. Horton, Effect of boron on grain-boundaries in Ni 3 Al, Acta Metall. 33 (2) (1985) 213–229.
[9] H.L. Tuller, Ionic conduction in nanocrystalline materials, Solid State Ionics 131 (2000) 143–157.
[10] A. Atkinson, R.I. Taylor, Ni along grain boundaries in nickel oxide, Philos. Mag. A 43 (4) (1981) 979–998.
[11] Y.R. Kolobov, A.G. Lipnitskii, I.V. Nelasov, G.P. Grabovetskaya, Investigations and computer simulations of the intergrain diffusion in submicro-and nanocrystalline metals, Russ. Phys. J. 51 (4) (2008) 385–399.
[12] M.I. Buckett, K.L. Merkle, Determination of grain boundary volume expansion by HREM, Ultramicroscopy 56 (1–3) (1994) 71–78.
[13] U. Dahmen, S. Paciornik, I.G. Solorzano, J.B. Vandersande, HREM analysis of structure and defects in a Σ 5(210) grain boundary in rutile, Interface Sci. 2 (1994) 125–136.
[14] E.M. Steyskal, B. Oberdorfer, W. Sprengel, M. Zehetbauer, R. Pippan, R. Würschum, Direct experimental determination of grain boundary excess volume in metals, Phys. Rev. Lett. 108 (5) (2012) 055504.
[15] B. Oberdorfer, D. Setman, E.M. Steyskal, A. Hohenwarter, W. Sprengel, M. Zehetbauer, R. Pippan, R. Würschum, Grain boundary excess volume and defect annealing of copper after high-pressure torsion, Acta Mater. 68 (100) (2014) 189–195.
[16] W.T. Read, W. Shockley, Dislocation models of crystal grain boundaries, Phys. Rev. 78 (1950) 275–289.
[17] A.D.L. Claire, The analysis of grain boundary diffusion measurements, Br. J. Appl. Phys. 14 (6) (1963) 351–356.
[18] D. Brandon, The structure of high-angle grain boundaries, Acta Metall. 14 (11) (1966) 1479–1484.
[19] M.A. Meyers, A. Mishra, D.J. Benson, M.A. Meyers, A.,B.D.J. Mishra, Mechanical properties of nanocrystalline materials, Prog. Mater. Sci. 51 (4) (2006) 427–556.
[20] C. Schmidt, M.W. Finnis, F. Ernst, V. Vitek, Theoretical and experimental investigations of structures and energies of Σ = 3, [112] tilt grain boundaries in copper, Philos. Mag. A 77 (5) (1998) 1161–1184.
[21] O.H. Duparc, S. Poulat, A. Larere, J. Thibault, L. Priester, High-resolution transmission electron microscopy observations and atomic simulations of the structures of exact and near Σ = 11, {332} tilt grain boundaries in nickel, Philos. Mag. A 80 (4) (2000) 853–870.
[22] A. Morawiec, Method to calculate the grain boundary energy distribution over the space of macroscopic boundary parameters from the geometry of triple junctions, Acta Mater. 48 (13) (2000) 3525–3532.
[23] J. Li, S.J. Dillon, G.S. Rohrer, Relative grain boundary area and energy distributions in nickel, Acta Mater. 57 (14) (2009) 4304–4311.
[24] M.P. Seah, E.D. Hondros, Grain boundary segregation, Proc. R. Soc. A Math. Phys. Eng. Sci. 335 (1601) (1973) 191–212.
[25] M.P. Seah, Grain boundary segregation and the T-t dependence of temper brittleness, Acta Metall. 25 (1977) 345–357.
[26] P. Lejček, S. Hofmann, Thermodynamics and structural aspects of grain boundary segregation, Crit. Rev. Solid State Mater. Sci. 20 (1) (1995) 1–85.
[27] T. Mütschele, R. Kirchheim, Segregation and diffusion of hydrogen in grain boundaries of palladium, Scr. Metall. 21 (c) (1987) 135–140.
[28] N. Gokon, M. Kajihara, Occurrence of faceting for [110] symmetric tilt boundaries in Cu doped with Bi, Mater. Trans. 49 (11) (2008) 2584–2590.
[29] E. Budke, T. Surholt, S. Prokofjev, L. Shvindlerman, C. Herzig, Tracer diffusion of Au and Cu in a series of near Σ = 5(310)[001] symmetrical Cu tilt grain boundaries, Acta Mater. 47 (2) (1999) 385–395.
[30] D. Wolf, Correlation between the energy and structure of grain boundaries in b.c.c. metals. II. Symmetrical tilt boundaries, Philos. Mag. A 62 (4) (1990) 447–464.
[31] M.S. Daw, S.M. Foiles, M.I. Baskes, The embedded-atom method: a review of theory and applications, Mater. Sci. Rep. 9 (7) (1993) 251–310.
[32] R. Wu, A.J. Freeman, G.B. Olson, First principles determination of the effects of phosphorus and boron on iron grain boundary cohesion, Science 265 (5170) (1994) 376–380.
[33] J. Rittner, D. Seidman, ⟨110⟩ Symmetric tilt grain-boundary structures in Fcc metals with low stacking-fault energies, Phys. Rev. B 54 (10) (1996) 6999–7015.
[34] I. Dawson, P.P. Bristowe, M.M.-H.M.M.-H. Lee, M. Payne, J. White, M. Segall, First-principles study of a tilt grain boundary in rutile, Phys. Rev. B 54 (19) (1996) 13727–13733.
[35] R.J. Kurtz, H.L. Heinisch, The effects of grain boundary structure on binding of He in Fe, J. Nucl. Mater 329–333 (2004) 1199–1203.
[36] D. Spearot, M. Tschopp, K. Jacob, D. Mcdowell, Tensile strength of ⟨ 100⟩ and ⟨ 110⟩ tilt bicrystal copper interfaces, Acta Mater. 55 (2) (2007) 705–714.
[37] K.P. McKenna, F. Hofer, D. Gilks, V.K. Lazarov, C. Chen, Z. Wang, Y. Ikuhara, Atomic-scale structure and properties of highly stable antiphase boundary defects in Fe3O4, Nat. Commun. 5 (2014) 5740.
[38] J.A. Moriarty, J.F. Belak, R.E. Rudd, P. Söderlind, F.H. Streitz, L.H. Yang, Quantum-based atomistic simulation of materials properties in transition metals, J. Phys. Condens. Matter 14 (11) (2002) 2825–2857.
[39] M.A. Tschopp, G.J. Tucker, D.L. McDowell, Structure and free volume of ⟨110⟩ symmetric tilt grain boundaries with the E structural unit, Acta Mater. 55 (11) (2007) 3959–3969.
[40] Y. Mishin, M. Asta, J. Li, Atomistic modeling of interfaces and their impact on microstructure and properties, Acta Mater. 58 (4) (2010) 1117–1151.
[41] H. Aaron, G. Bolling, Free volume as a criterion for grain boundary models, Surf. Sci. 31 (1972) 27–49.
[42] L. Zhang, X. Shu, S. Jin, Y. Zhang, G.-H. Lu, First-principles study of He effects in a bcc Fe grain boundary: site preference, segregation and theoretical tensile strength, J. Phys. Condens. Matter 22 (37) (2010) 375401.
[43] L. Zhang, C.C. Fu, G.H. Lu, Energetic landscape and diffusion of He in α-Fe grain boundaries from first principles, Phys. Rev. B 87 (2013) 1–11.
[44] W.-T. Geng, A.J. Freeman, G.B. Olson, Y. Tateyama, T. Ohno, Hydrogen-promoted grain boundary embrittlement and vacancy activity in metals: insights from Ab initio total energy calculations, Mater. Trans. 46 (4) (2005) 756–760.
[45] M. Yamaguchi, K.I. Ebihara, M. Itakura, T. Kadoyoshi, T. Suzudo, H. Kaburaki, First-principles study on the grain boundary embrittlement of metals by solute segregation: Part II. metal (Fe, Al, Cu)-hydrogen (H) systems, Metall. Mater. Trans. A Phys. Metall. Mater. Sci. 42 (2) (2011) 330–339.
[46] K.N. Solanki, M.A. Tschopp, M.A. Bhatia, N.R. Rhodes, Atomistic investigation of the role of grain boundary structure on hydrogen segregation and embrittlement in α-Fe, Metall. Mater. Trans. A Phys. Metall. Mater. Sci. 44 (3) (2013) 1365–1375.
[47] H. Bolt, V. Barabash, W. Krauss, J. Linke, R. Neu, S. Suzuki, N. Yoshida, Materials for the plasma-facing components of fusion reactors, J. Nucl. Mater. 329–333 (2004) 66–73.
[48] I. Bergenti, V. Dediu, M. Cavallini, E. Arisi, A. Riminucci, C. Taliani, Properties of thin manganite films grown on semiconducting substrates for spintronics applications, Curr. Appl. Phys. 7 (1) (2007) 47–50.
[49] B. Poudel, Q. Hao, Y. Ma, Y. Lan, A. Minnich, B. Yu, X. Yan, D. Wang, A. Muto, D. Vashaee, X. Chen, J. Liu, M.S. Dresselhaus, G. Chen, Z. Ren, High-thermoelectric performance of nanostructured bismuth antimony telluride bulk alloys, Science 320 (5) (2008) 634–638.
[50] S.J. Zinkle, J.T. Busby, Structural materials for fission & fusion energy, Mater. Today 12 (11) (2009) 12–19.
[51] M. Shiga, M. Yamaguchi, H. Kaburaki, Structure and energetics of clean and hydrogenated Ni surfaces and symmetrical tilt grain boundaries using the embedded-atom method, Phys. Rev. B 68 (24) (2003) 245402.
[52] M.R. Hestenes, E. Stiefel, Method of conjugate gradients for solving linear systems, J. Res. Nat. Bur. Stand 49 (6) (1952) 409–436.
[53] E.A. Holm, D.L. Olmsted, S.M. Foiles, Comparing grain boundary energies in face-centered cubic metals: Al, Au, Cu and Ni, Scr. Mater. 63 (9) (2010) 905–908.
[54] S. Ratanaphan, D.L. Olmsted, V.V. Bulatov, E.A. Holm, A.D. Rollett, G.S. Rohrer, Grain boundary energies in body-centered cubic metals, Acta Mater. 88 (2015) 346–354.
[55] S.K. Wallace, K.P. McKenna, Grain boundary controlled electron mobility in polycrystalline titanium dioxide, Adv. Mater. Interfaces 1 (5) (2014) 1400078.

[56] Z. Wang, M. Saito, K.P. McKenna, L. Gu, S. Tsukimoto, A.L. Shluger, Y. Ikuhara, Atom-resolved imaging of ordered defect superstructures at individual grain boundaries, Nature 479 (7373) (2011) 380–383.
[57] K. McKenna, A. Shluger, The interaction of oxygen vacancies with grain boundaries in monoclinic HfO2, Appl. Phys. Lett. 95 (22) (2009) 8–11.
[58] S. Plimpton, Fast parallel algorithms for short-range molecular dynamics, J. Comp. Phys. 117 (1) (1995) 1–19.
[59] G. Ackland, G. Tichy, V. Vitek, M. Finnis, Simple n-body potentials for the noble metals and nickel, Philos. Mag. A 56 (6) (1987) 735–756.
[60] F. Cleri, V. Rosato, Tight-binding potentials for transition metals and alloys, Phys. Rev. B 48 (1) (1993) 22–33.
[61] A.P. Sutton, J. Chen, Long-range finnis–sinclair potentials, Philos. Mag. Lett. 61 (3) (1990) 139–146.
[62] G.J. Ackland, D.J. Bacon, A.F. Calder, T. Harry, Computer simulation of point defect properties in dilute FeCu alloy using a many-body interatomic potential, Philos. Mag. A 75 (3) (1997) 713–732.
[63] F. Birch, Finite elastic strain of cubic crystals, Phys. Rev. 71 (11) (1947) 809–824.
[64] M.I. Mendelev, S. Han, D.J. Srolovitz, G.J. Ackland, D.Y. Sun, M. Asta, Development of new interatomic potentials appropriate for crystalline and liquid iron, Philos. Mag. 83 (35) (2003) 3977–3994.
[65] W. Gale, T. Totemeier, Smithells Metals Reference Book, Butterworth-Heinemann, 2003.
[66] W. B. Pearson, A Handbook of Lattice Spacings and Structures of Metals and Alloys, Elsevier (Republished 2013).
[67] H. Ledbetter, E. Naimon, Elastic properties of metals and alloys. ii. Copper, J. Phys. Chem. Ref. Data 3 (4) (1974) 897–935.
[68] H. Ledbetter, R.P. Reed, Elastic properties of metals and alloys, i. iron, nickel, and iron-nickel alloys, J. Phys. Chem. Ref. Data 2 (3) (1973) 531–618.
[69] P. Hohenberg, W. Kohn, The inhomogeneous electron gas, Phys. Rev. 136 (1964) B864.
[70] W. Kohn, L.J. Sham, Self consistent equations including exchange and correlation effects, Phys. Rev. 385 (1965) A1133–A1138.
[71] S.J. Clark, M.D. Segall, C.J. Pickard, P.J. Hasnip, M.I.J. Probert, K. Refson, M.C. Payne, First principles methods using CASTEP, Z. für Krist. 220 (2005) 567–570.
[72] J.P. Perdew, K. Burke, M. Ernzerhof, Generalized gradient approximation made simple, Phys. Rev. Lett. 77 (18) (1996) 3865.
[73] R.H. Byrd, J. Nocedal, R.B. Schnabel, Representations of quasi-Newton matrices and their use in limited memory methods, Math. Program 63 (1994) 129–156.
[74] V. Vitek, D. Smith, R. Pond, Structure of tilt grain boundaries in bcc metals, Philos. Mag. A (5) (1980) 37–41.
[75] Gui Jin Wang, A. Sutton, V. Vitek, A computer simulation study of ⟨001⟩ and ⟨111⟩ tilt boundaries: the multiplicity of structures, Acta Metall. 32 (7) (1984) 1093–1104.
[76] F. Berthier, B. Legrand, G. Tréglia, New structures and atomistic analysis of the polymorphism for the $\Sigma = 5$ (210) [001] tilt boundary, Interface Sci. 8 (2000) 55–69.
[77] M. Sørensen, Y. Mishin, A. Voter, Diffusion mechanisms in Cu grain boundaries, Phys. Rev. B 62 (6) (2000) 3658–3673.
[78] A. Suzuki, Y. Mishin, Atomistic modeling of point defects and diffusion in copper grain boundaries, Interface Sci. 11 (2003) 131–148.
[79] A.Y. Lozovoi, A.T. Paxton, M.W. Finnis, Structural and chemical embrittlement of grain boundaries by impurities: a general theory and first-principles calculations for copper, Phys. Rev. B 74 (15) (2006) 155416.
[80] H. Jang, D. Farkas, Interaction of lattice dislocations with a grain boundary during nanoindentation simulation, Mater. Lett. 61 (3) (2007) 868–871.
[81] N. Gao, C.C. Fu, M. Samaras, R. Schäublin, M. Victoria, W. Hoffelner, Multiscale modelling of bi-crystal grain boundaries in bcc iron, J. Nucl. Mater. 385 (2) (2009) 262–267.
[82] D. Terentyev, X. He, Dimensionality of interstitial He migration in ⟨110⟩ tilt grain boundaries in α-Fe, Comput. Mater. Sci. 49 (4) (2010) 858–864.
[83] T. Frolov, D.L. Olmsted, M. Asta, Y. Mishin, Structural phase transformations in metallic grain boundaries, Nat. Commun. 4 (2013) 1899.
[84] D.L. Olmsted, S.M. Foiles, E.A. Holm, Survey of computed grain boundary properties in face-centered cubic metals: I. grain boundary energy, Acta Mater. 57 (13) (2009) 3694–3703.
[85] R.I. Masel, Principles of Adsorption and Reaction on Solid Surfaces, vol. 3, John Wiley & Sons, 1996.
[86] J. Snyder, Map Projections—a Working Manual, 1987.
[87] A.P. Sutton, R.W. Balluffi, Interfaces in Crystalline Materials, Oxford University Press, Oxford, 1995.